JOURNAL OF AIRCRAFT
Vol. 37, No. 3, May–June 2000

Numerical Simulation of Transonic Flow over Wing-Mounted Twin-Engine Transport Aircraft

Jie Li,* Fengwei Li,† and Qin E‡
Northwestern Polytechnical University, Xi'an, 710072 Shaanxi, People's Republic of China

A numerical method has been developed for computing the flowfield around advanced transport aircraft with wing-mounted nacelles. The method is based on a multiblock point-matched grid-generation approach combined with zonal solving strategy for complex flowfield. In this study the flowfield is divided into a number of nonoverlapped blocks by a cutout technique. H-type grids are generated independently in each block using an elliptic grid-generation method, in which the control of the grid quality is accomplished by the forcing-function technique of Hilgenstock. The flowfield is simulated by solving the Euler equations. An explicit three-stage Runge–Kutta algorithm based on the Jameson's finite volume scheme for the Euler equations has been developed that is applied to the multiregion H-type grids. The present method has been applied to isolated powered engine nacelles and complex transport aircrafts consisting of low-wing/fuselage with wing-mounted pylon/nacelles. On the wing surfaces the viscous effects are simulated by the employment of the viscous/inviscid interaction (VII) technique of two-dimensional strip boundary layer. In this study the boundary-layer program uses an integral method to calculate turbulent boundary layers. With the concept of an equivalent inviscid flow, the model of blowing velocity is employed in the VII technique. The effect of the boundary layer on the outer inviscid flow is represented through a transpiration boundary condition derived from the boundary-layer parameters. The main benefit of this treatment is that the grid is generated only once in overall computing procedure. Computational results and comparisons with experimental data are presented. The good agreement indicates that the present method is effective in predicting the flows about powered engine nacelles and/or complex transport aircrafts.

Introduction

WITH the increment of the civil aircraft cruise speed, the installation of the propulsion system has become increasingly important. It was proven by practice that the interaction between the wing-mounted engine system and the airframe could have a significant impact on the aerodynamic performance of an aircraft.[1–5] From a historical point of view, the interference drag and other negative effects relative to the engine installation on the high subsonic transport aircraft were major factors that resulted in deterioration of aircraft aerodynamic characteristic.[6] For example, the engine installation effects on an advanced transport aircraft were spreading over the major part of the wing span and did not limit within the local region nearby the pylon and nacelle.[4–6] An increase in induced drag could hence be caused by the change in the wing span loading because of the presence of the propulsion system.

On the other hand, the quest for improved propulsive efficiency for commercial transport aircraft in the form of the lower specific fuel consumption has led to the further development of high-bypass-ratio turbofan engines.[5] Consequently, the new concept engines result in larger fan diameters. For wing-mounted engines the problem is additionally aggravated by the fact that the severe restrictions placed by the minimum ground clearance and avoidance of increasing length of the landing gear hence require a closer coupling of engine and wing. Therefore, the aerodynamic interference effects on airframe/propulsion integration will become stronger. An inefficient installation design could pose the risk that the aircraft performance gains obtained from propulsive efficiency of new engine types are easily negated or even overruled by losses caused by detrimental airframe/propulsion interference effects.

Overall optimal design and integration of the propulsion system into the airframe will result in an enhanced performance of the whole aircraft. Nowadays, the successful integration of the propulsion system on modern aircraft becomes a very challenging target and an important feature in the design and development of advanced technology aircraft.[6]

In context with the high requirements for aerodynamic performance of advanced civil aircraft and the strong interactions existing between the airframe and the propulsion system, the accurate prediction and careful analysis of the engine installation effects are needed to assess and further improve the whole aircraft performance in the early or even all phases of the design process.

The experimental and theoretical investigations are effective approaches to attack the aforementioned problems. Historically, the integration of propulsion systems was carried out principally by the experimental approach. The main problems using this way to optimize the airframe/propulsion integration are the very long process and the enormous cost as well as the difficulty to localize the origin of the problems in order to find the right solutions. With the significant advances achieved in supercomputer technology and computational fluid dynamics (CFD) over the past two decades, the numerical simulation of the flowfield around twin-engine transport aircraft has become possible. At present, numerical methods have the capability to solve independently many propulsion integration design problems and have been frequently used to gain insight into the elements playing a role in the interference process.[1–7]

Timeliness is all important in the design and development of civil aircraft. The aerodynamic design is never the result of a single design process, but rather of a sequential refinement. On this account, the CFD approach has the advantages that the wind-tunnel testing does not have. CFD technology can give designer the freedom to look at many different design options early and decide if a change is beneficial. The best and most promising changes can then be targeted for always limited resources, resulting in fewer designs going to test, with subsequent overall cost savings.

Owing to its unique advantages, CFD becomes an efficient approach for the investigation of airframe/propulsion integration. The value of CFD is founded on the capability to describe with sufficient accuracy the physical phenomena within the available time. To deal with these challenges, there is an urgent need to develop and validate computational tools aimed at the prediction of interference

Received 9 August 1999; revision received 26 October 1999; accepted for publication 31 October 1999. Copyright © 2000 by the American Institute of Aeronautics and Astronautics, Inc. All rights reserved.

*Lecturer, Department of Aircraft Engineering, P.O. Box 114.
†Professor, Department of Aircraft Engineering, P.O. Box 114. Member AIAA.
‡Professor, Department of Aircraft Engineering, P.O. Box 114.

effects caused by airframe/propulsion integration. Hence, great efforts must be made in the development and calibration of CFD method, which could become a reliable substitute for the expensive and time-consuming wind-tunnel testing investigation.

Because of the great generality of the flow-solving methods, it can be argued in a certain sense that the main difficulty and task in numerical simulation of a more complex flowfield are to develop a means to produce a high-quality grid in a fast and efficient way. This is especially true when the influence of different components of an advanced transport aircraft on the flowfield is to be investigated. When the CFD approach is employed to study the airframe/propulsion integration, the generation of a high-quality body-fitted structured grid having sufficient smoothness and orthogonality becomes the prerequisite and the key for this problem.

This paper focuses on the numerical simulation of the flowfield over advanced twin-engine transport aircraft. The grid system is generated using a multiblock matched grid technique. The flowfield is simulated by solving the Euler equations. On the wing surfaces the viscous effects are simulated by the employment of the viscous/inviscid interaction (VII) technique of a two-dimensional strip boundary layer.

The capability of the present method has been demonstrated in the analysis of flows about isolated powered engine nacelles and complex transport aircrafts consisting of low-wing/fuselage with wing-mounted pylon/nacelles. Comparisons of numerical results and experimental data show good agreement, which indicates that the present method is effective and robust in predicting the flows about powered engine nacelles and/or advanced transport aircrafts.

Multiblock Grid-Generation Technique

For a general transport aircraft with wing-mounted engine nacelles, it is usually difficult to produce a single-block, high-quality body-fitted orthogonal grid with smooth and well-distributed grid spacing in the field. To overcome such difficulty, a multiblock grid approach combined with a zonal flow solver is employed to generate the grid about complex transport aircraft.

Choice of Grid Topology

The important step in the multiblock grid approach for complex aircraft configuration is to decide about a global grid topology that allows the necessary subgrids around the different components to be easily embedded. The choice of an appropriate grid topology should be done in a way that a change of engine type or position should require as few changes in the overall grid as possible so that the effort necessary for the investigation of a new engine concept or different positions will be kept to a minimum.

To achieve this purpose, an H-type grid structure in streamwise direction and an O-type structure in spanwise direction are employed for the global grid around the wing/body combination. Thus, changes in the grid caused by different engine types or positions are limited to a confined region around the engine nacelle itself.

Zonal Solving Strategy for Complex Flowfield

With the employment of H-type grid topology structure, zonal solving strategy can be adopted to simplify the numerical simulation of the complex flowfield because of its flexibility in handling flowfields around complex configurations.

For the wing/body/pylon/nacelle case the flowfield is partitioned into two major zones, an inner region for intake/exhaust flow of engine nacelle and an outer region for the wing/body flowfield, as sketched in Fig. 1. This decomposition for the domain is accomplished by introducing the nacelle inlet and exit tubes represented by the dashed lines, which extend to the far field upstream and downstream.

The zonal, multiblock structure combined with the use of H-type topology allows the grid-generation technique to be applied for complex configurations in a fast and flexible way.

Multiblock Point-Matched Grid Technique

The basic idea of the multiblock grid technique is to decompose the domain into different appropriate blocks, and then subgrids are generated separately in each block and patched smoothly along common boundaries to form the global grid for the complete aircraft. Thus, a one-to-one correspondence of grid points on both abutting block boundaries will be maintained. The philosophy for the decomposition of main domain for complex wing-mounted transport aircraft can be described as follows.

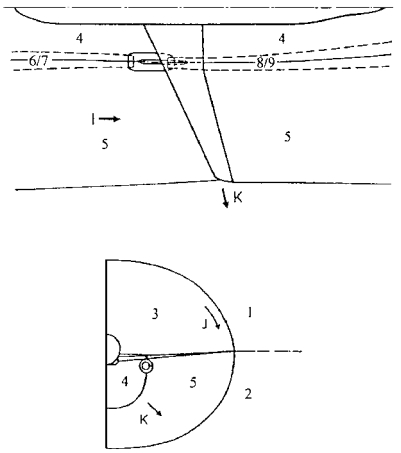

Fig. 1 Flowfield decomposition for wing/body/pylon/nacelle configuration.

Starting from a simple grid around base configuration like a wing/body combination, the grid of more complex configuration can be generated using a cutout technique. Local blocks are cut out of the wing/body grid and filled with a new grid that describes the new components. Such a local block grid system must be required to fit to the boundaries of the cutout block.

In this study pylon and nacelle are integrated into the global grid by introducing a subblock containing these components. After generating the global wing/body grid, a specified region has to be cut out of the global grid to allow the substitution of the subgrid containing the pylon and nacelle. The corresponding coordinate lines of the global wing/body grid together with the engine inlet/exit tubes as well as pylon/engine nacelle itself form the boundaries of this subblock. If the outer boundaries of this subgrid have then to be adapted to smoothly match the boundaries of the cutout region of the global grid, the final patched grid will be smooth and continuous. Using the grid-generation method described in the next section, this can be easily achieved by prescribing the grid angles consistent across the common boundaries between abutting blocks.

The topology for the subgrid inside the engine nacelle is an H-type structure in streamwise direction and a polar grid topology (O-type) with respect to the engine axis in circumferential direction. (Figure 9 gives a front view of the field grids at different stations along the body axis direction, which shows the resulting topology for the preceding procedure.)

Elliptic Grid-Generation Method

The global grid about the wing/body combination and the subgrids around/inside the engine nacelle are mainly obtained by using the elliptic grid-generation method with forcing-function control.[8,9] The symmetric successive overrelaxation (SSOR) technique is adopted to solve the elliptic equations, which are given in Ref. 9.

Forcing-Function Control Technique

The forcing-function control technique of Hilgenstock[9] is employed in this work. This method is an iterative procedure that adjusts the boundary forcing functions to meet a prescribed angle (spacing) constraint at the boundary. The main idea of this technique is to use the difference between a desired angle (spacing) and the actual angle (spacing) during the iteration to estimate the corrections to be added to the forcing-function terms. The forcing functions are

incremented from some initial values based on the local relative angle and/or spacing error. The update procedure then becomes

$$\varphi_P^{n+1} = \varphi_P^n + \Delta\varphi_P^{n+1}, \qquad \varphi_Q^{n+1} = \varphi_Q^n + \Delta\varphi_Q^{n+1}$$
$$\varphi_R^{n+1} = \varphi_R^n + \Delta\varphi_R^{n+1} \tag{1}$$

where the $\Delta\varphi_P$, $\Delta\varphi_Q$, and $\Delta\varphi_R$ are computed depending on whether they are controlling the angle or spacing at a given boundary.

To avoid excessively large values for the corrections, the tanh function is used to damp the corrections. The corrections to the forcing functions can then be expressed in the following manner:

$$\Delta^{n+1} = \pm\tanh\left(\frac{f_{\text{desired}} - f_{\text{actual}}}{f_{\text{desired}}}\right) \tag{2}$$

where f denotes the angle or spacing. The correction terms should change the sign from the inner boundary to the outer boundary.

With the employment of the forcing-function control technique, full control over grid angle and/or spacing with respect to any or all boundaries of the domain can be achieved. These characteristics of the present algorithm are especially important for the multiblock grid approach. With the forcing-function control technique the grid lines can be easily matched along the common boundaries between abutting blocks.

Numerical Procedure

The numerical approach to generate the grid consists of the following steps: 1) Generate an initial grid by an algebraic method based on transfinite interpolation. 2) Assume values of the forcing-function terms at the boundaries. 3) Change the forcing-function terms at the boundaries by Eq. (1) so that they are closer to the values needed for the desired grid. 4) Interpolate these new forcing-function terms between the two boundary surfaces into the field along ξ, η, ζ directions, respectively. 5) Solve the elliptic system by SSOR technique. Steps 3 to 5 are then repeated until the desired grid is reached.

The iteration process described in step 5 is called the inner iteration, whereas the iteration 3 to 5 is called the outer iteration. A change of forcing-function terms occurs only in the outer iteration while in the inner iteration the forcing-function terms are kept constants.

Euler Flow Solver

The unsteady, three-dimensional Euler equations in integral form are solved by using an explicit three-stage Runge–Kutta scheme with a local time step. Details of the numerical algorithm can be found in Refs. 10 and 11. Implicit residual smoothing and enthalpy-damping techniques have been employed to accelerate the convergence. For powered engine nacelle simulation, in which the outer flowfield and the nacelle exhaust flow have different total enthalpy, the enthalpy-damping technique is not used in the case of powered simulation. In the present method the Euler flow solver has been structured to allow the analysis of complex flow within the framework of multiregions.

Interactive Boundary-Layer Method

The VII technique is applied on the wing surfaces by two-dimensional strip theory to account for viscous effects. The boundary layer over the fuselage and pylon/nacelle surfaces is not calculated. Because the chordwise grid lines on the wing surfaces are nearly aligned with streamlines, the two-dimensional strip theory can be applied along cell face centers at a series of spanwise stations in the framework of central finite volume scheme.

Integral Boundary-Layer Equations

The two-dimensional, compressible integral boundary-layer equations, as shown in Ref. 12, the integral momentum equation, and the integral mean-flow kinetic energy equation are employed:

$$\frac{1}{\rho_e u_e^2}\frac{\mathrm{d}}{\mathrm{d}S}\left(\rho_e u_e^2\theta\right) + \frac{\delta^*}{u_e}\frac{\mathrm{d}u_e}{\mathrm{d}S} = \frac{C_f}{2} \tag{3}$$

$$\frac{1}{2\rho_e u_e^3}\frac{\mathrm{d}}{\mathrm{d}S}\left(\rho_e u_e^3\theta^*\right) + \frac{\delta^{**}}{u_e}\frac{\mathrm{d}u_e}{\mathrm{d}S} = \frac{C_f}{2}D \tag{4}$$

where S is the distance along the boundary-layer strips of the wing surfaces and the subscript e refers to the inviscid flow quantities evaluated at the edge of the boundary layer. The velocity at the edge of the boundary layer u_e is known and can be provided by the Euler analysis. The quantities δ^*, θ, δ^{**}, and θ^* are the displacement, momentum, density, and kinetic energy thickness, respectively. The variable C_f is the skin-friction coefficient, and D is the dissipation coefficient, which can be expressed as

$$D = \frac{1}{\rho_e u_e^2}\int_0^\infty \tau\frac{\partial}{\partial y}\left(\frac{u}{u_e}\right)\mathrm{d}y \tag{5}$$

in which τ is the total shear stress.

Because there exist more unknowns than the equations, the solution of Eqs. (3) through (5) requires the closure of the set of equations. Here, closure is obtained by employing a series of relations given by Whitfield in Refs. 12 and 13.

The two-dimensional integral boundary-layer equations are solved using a fourth-order Runge–Kutta method.

Blowing Velocity Model

The important integral quantity δ^* can be expressed as

$$\delta^* = \frac{1}{\rho_e u_e}\int_0^\delta (\rho_e u_e - \rho u)\,\mathrm{d}y \tag{6}$$

The displacement thickness has the physical interpretation of being the distance the external inviscid streamlines are displaced by the boundary layer. Two approaches can be used for coupling the inviscid and viscous flow solutions, displacement approach, and blowing approach. The displacement approach requires a robust grid movement scheme, whereas the wing geometry and the grid system remain unchanged in the blowing approach.

The interactive boundary-layer scheme used in this study employs the surface blowing velocity to account for the effect of displacement thickness. In this case the effect of the boundary layer on the inviscid flow is represented through a transpiration boundary condition derived from the boundary-layer parameters.

With the blowing approach the surface blowing velocity V_n, which will be the boundary condition on the wing surfaces in inviscid flow calculation, is computed from the boundary-layer edge values of density ρ_e and velocity u_e and the displacement thickness δ^* as follows:

$$V_n = \frac{1}{\rho_e}\frac{\mathrm{d}}{\mathrm{d}S}\left(\rho_e u_e \delta^*\right) \tag{7}$$

Use of Eq. (7) affects only the surface boundary condition in the inviscid calculation and thus does not require significient modifications to the Euler solver.

Viscous/Invscid Interaction Procedure

The interactive procedure developed for the airfoil boundary-layer calculation in Ref. 14 is applied here for the wing boundary-layer calculation. As shown in the flowchart Fig. 2, the iteration procedure consists of the following steps:

1) Give an initial guess for the displacement thickness δ^*.

2) Input δ^* to the inverse boundary-layer calculation to obtain the viscous edge velocity u_{ev} and deduce the density ρ_{ev} from the viscous edge velocity.

3) Compute the blowing velocity at the wing surfaces by Eq. (7).

4) Perform the Euler solver to obtain the inviscid surface tangential velocity.

5) Compute the new displacement thickness distribution. By using the inviscid surface tangential velocity as the edge velocity just outside the boundary layer, the new δ^* is obtained from the following update procedure including a relaxation parameter ω:

$$\delta^{*(n+1)} = \delta^{*(n)} + \omega\delta^{*(n)}\left(u_{\text{ev}}^{(n)}\big|\ u_{\text{ei}} - 1\right) \tag{8}$$

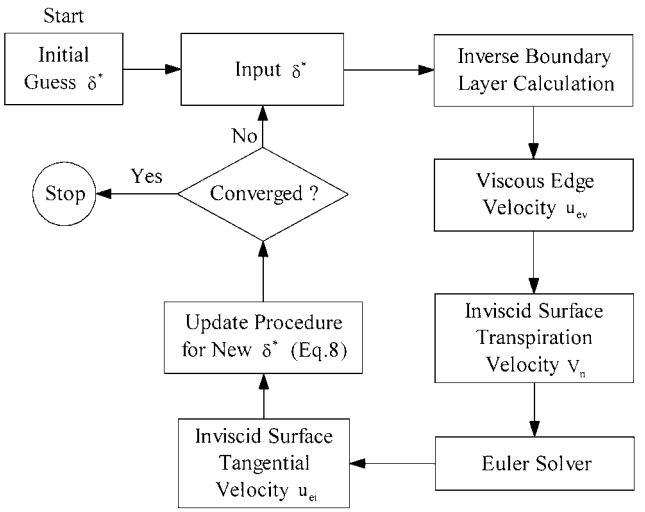

Fig. 2 Flowchart of viscous/inviscid interaction.

This update procedure[15] for the displacement thickness is the key link that allows an inverse boundary-layer computation to be coupled with the Euler solver.

Steps 2 to 5 are then repeated until convergence is obtained when the new and old δ^* differ by less than a specified tolerance.

Starting from the 800th time step, the boundary-layer calculations are performed for each strip every 10 iterations during the time stepping of the Euler solver. After processing all strips the blowing velocity has been updated at cell face centers on the wing surfaces. For most calculations 1500 time steps are sufficient to get a converged solution.

Boundary Conditions and Simulation of Powered Engine Nacelle

To define the problem under consideration, the specification of appropriate boundary conditions is necessary. Various boundary condition types exist in this study: first the physical boundaries and second the artificial point-patched boundaries between abutting zones.

Far-Field Boundary Condition

At the far-field boundary some special boundary conditions must be imposed. First, these conditions must bring the information of the undisturbed flow into the computational domain. Second, the disturbance emanating from the model can propagate into the freestream without reflection. In this study the theory of characteristics is employed to construct the boundary conditions. Implementing details of far-field boundary conditions could be found in Ref. 10.

Body Surface Boundary Condition for Inviscid Flow

At the solid surface boundary for inviscid flow, the impermeable boundary condition is applied, i.e., the normal flux at the body surface is zero. Therefore, the static pressure needs to be solved only, which can be obtained from the field by extrapolation. Because the pressure is spread along the surface normal direction, the accuracy of the boundary treatment will be increased with the simplified computation when the grid lines are orthogonal to the body surfaces.

Wing Surface Boundary Condition in VII Technique

With the employment of the blowing approach, the no-flux boundary condition through a solid surface applied in the inviscid flow calculation is modified to allow a prescribed surface blowing velocity condition. At the wing surfaces the boundary condition is changed to enforce a normal blowing velocity, accounting for the addition or subtraction of mass flux through the surface to maintain the growth or decay of displacement thickness along the streamwise direction. In effect, these viscous surfaces are treated as flow through boundaries.

Zonal Boundary Condition

In this study the grid lines between abutting zones are smoothly point-matched together along the common artificial boundaries with a one-to-one correspondence of grid points. This treatment simplifies the communication of the flow information between abutting zones. The flux across each cell face at these algorithmic boundaries is physically continuous and conservative; the corresponding cell values are obtained from the appropriate cells of the neighboring zone in each computational region.

Fan Inlet Face Boundary Condition

The boundary condition at the fan inlet face should yield the mass flow, which is specified by the engine data at the flow condition to be evaluated.[16–19] The mass flow at the fan face is defined as

$$\dot{m}_{\text{fan}} = \rho_{\text{fan}} q_{\text{fan}} A_{\text{fan}} = \rho_\infty q_\infty A_\infty \tag{9}$$

The mass-flow ratio of the air-intake (MFR) can be specified as

$$\text{MFR} = \frac{A_\infty}{A_{\text{HL}}} = \frac{\rho_{\text{fan}}}{\rho_\infty}\frac{q_{\text{fan}}}{q_\infty}\frac{A_{\text{fan}}}{A_{\text{HL}}} \tag{10}$$

where A_{HL} is the cross-sectional area at highlight and A_{fan} is the fan face area.

The treatment of the fan inlet face boundary condition is very similar to inflow/outflow boundary conditions at the farfield by the characteristic theory. The only difference comes from the way in which the outside information is specified.

From Eq. (10) and the freestream total conditions, the outside information at the inlet can be easily prescribed. Equation (10) can be expressed in terms of Mach number at the fan M_{fan} and M_∞ using isentropic relations and one-dimensional energy conservation.

$$\text{MFR} = (A_{\text{fan}}/A_{\text{HL}}) M_{\text{fan}} \left\{1 + [(\gamma-1)/2] M_{\text{fan}}^2\right\}^{-[(\gamma+1)/2(\gamma-1)]} \times (\rho_0/\rho_\infty)(a_0/q_\infty) \tag{11}$$

$$\rho_0/\rho_\infty = \left\{1 + [(\gamma-1)/2] M_\infty^2\right\}^{1/(\gamma-1)} \tag{12}$$

$$a_0/q_\infty = \left\{[(\gamma-1)/2] + \left(1 \middle| M_\infty^2\right)\right\}^{\frac{1}{2}} \tag{13}$$

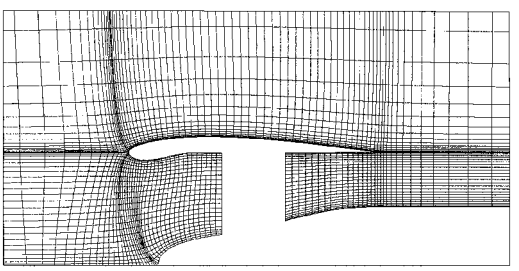

Fig. 3 Computational grid at meridian for CRUF model.

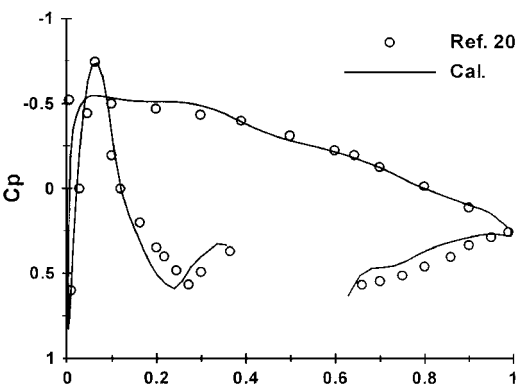

Fig. 4 Surface-pressure distributions along outer cowl, inlet cowl, and fan-jet cowl for CRUF model.

Equation (11) can be solved iteratively for M_{fan}. Then the other variables such as temperature, density, as well as static pressure at the fan face, can be determined from isentropic relations. These data are used to determine the boundary condition at the fan face using the same characteristic procedure as in the case of far-field conditions.

Jet-Exit Boundary Condition

Total pressure ratio (PR) and total temperature ratio (TR) of the exhausting jet along with MFR define the engine operation conditions.[16–19] These must be specified in the numerical simulation. In the real engine the inlet mass flow is divided into the fan jet and core jet flows. The fuel is added to the core jet flow. In the case of turbofan engine, the fuel mass is relatively small and can be neglected. Therefore, the fan jet and core jet mass fluxes can be specified by the bypass ratio (BR). Knowing the PR, TR, and the BR at the jet exits, the outside information can be readily prescribed as the case of the fan inlet face.

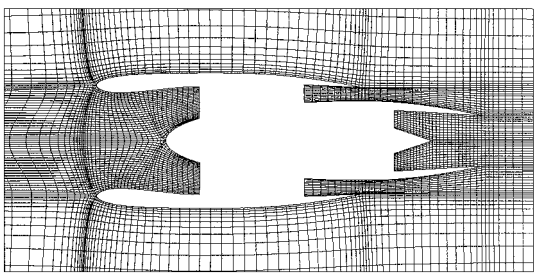

Fig. 5 Computational grid at meridian for TPS model.

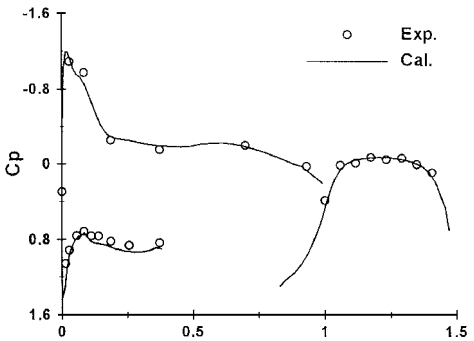

Fig. 6 Pressure distributions on outer cowl, fan-, and core-cowl surfaces for TPS model.

Numerical Results and Discussion

Flow Simulation of Isolated Powered Engine Nacelle

To verify the ability of present method for general powered engine nacelle simulation, two engine nacelle models were chosen for analyses by using the Euler solver.

Counter-Rotating Ultra-High-Bypass Fan Simulator (CRUF) Model[20]

This geometric configuration was taken from Ref. 20. The contour curves of this geometry and the computational grid at the meridian plane are shown in Fig. 3.

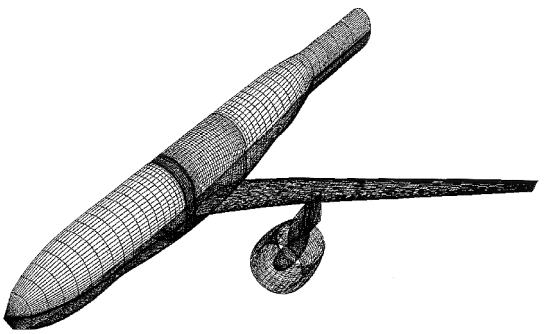

Fig. 8 Surface grid for low-wing transport model.

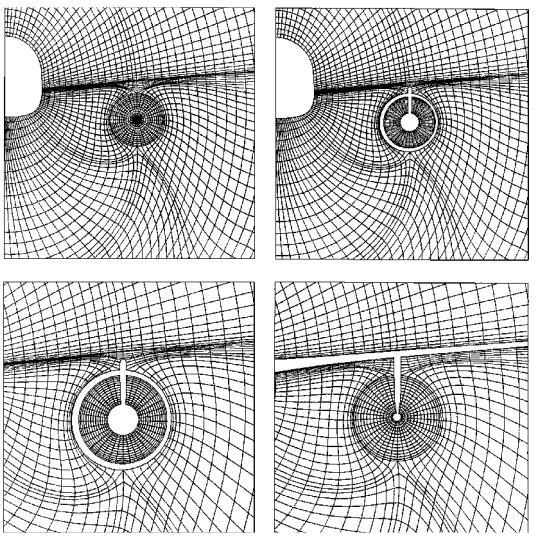

Fig. 9 Front view of field grids at different stations along body axis direction.

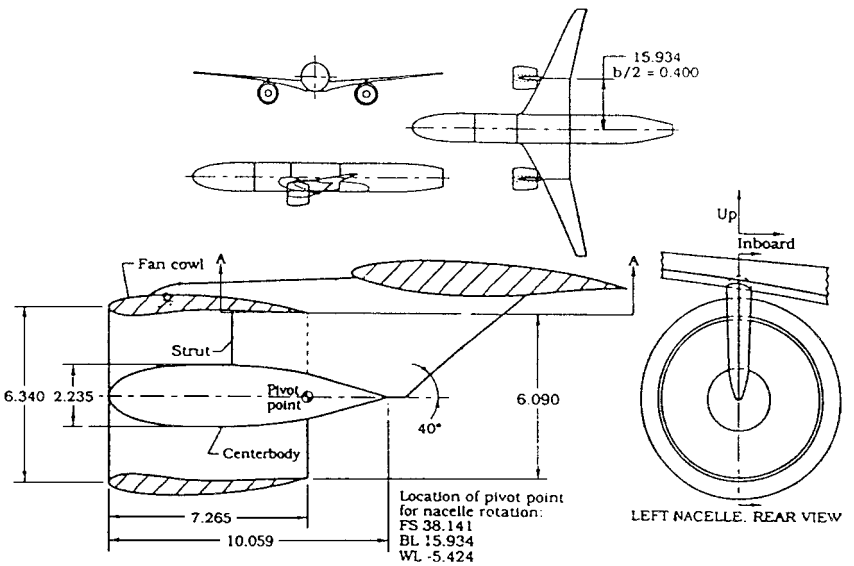

Fig. 7 Sketch of NASA TP-3168 low-wing transport model.

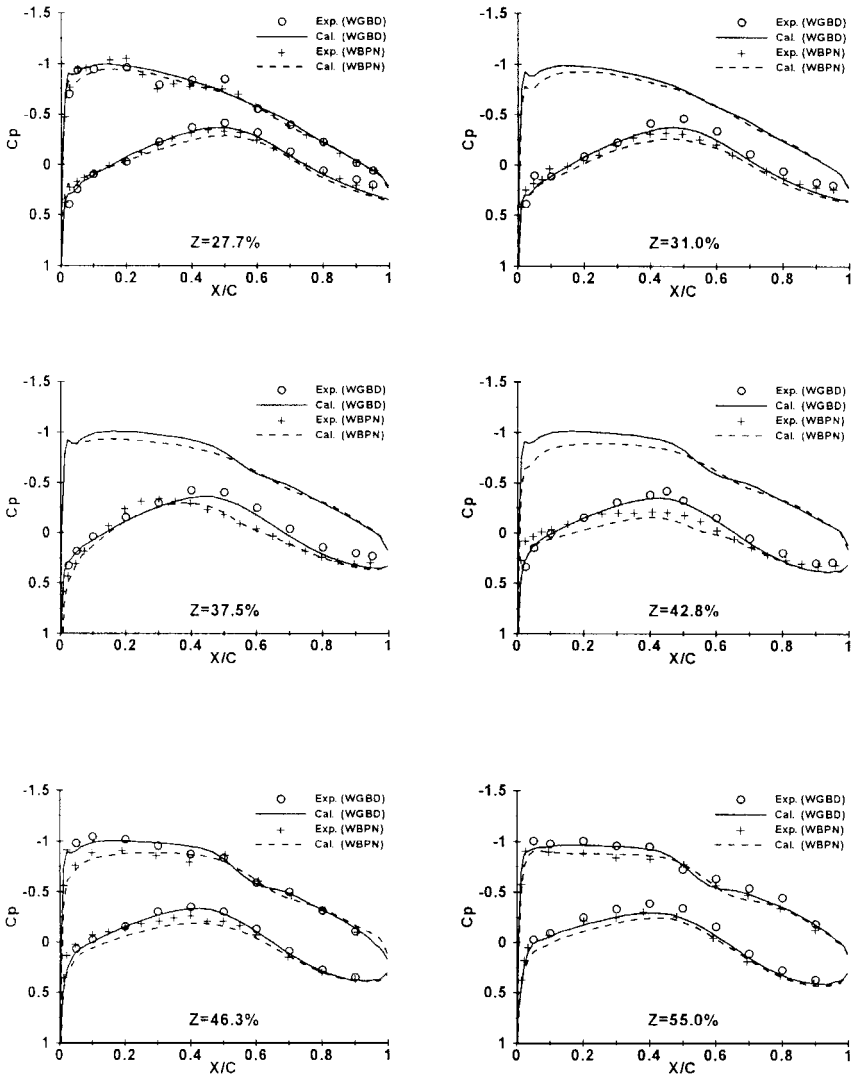

Fig. 10 Wing surface-pressure distributions for NASA TP-3168 model.

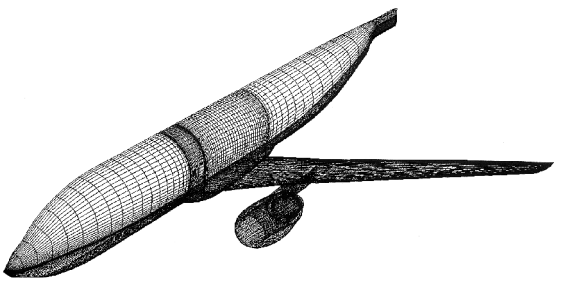

Fig. 11 Surface grid for AE100 transport aircraft model.

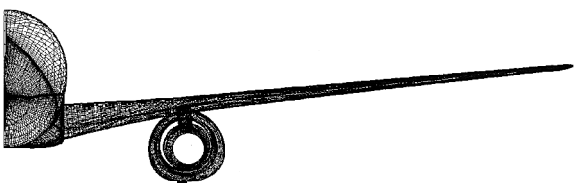

Fig. 12 Front view of surface grid for AE100 aircraft model.

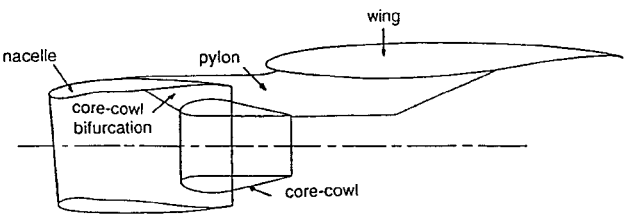

Fig. 13 Sketch of pylon/nacelle geometry.

The flow was analyzed at $M = 0.80$, $\alpha = 0.0$ deg with the engine conditions: MFR $= 0.914$, at the jet PR $= 1.0$ and TR $= 1.0$. The computational pressure distributions are compared with the Euler results of Ref. 20 along the outer cowl, inlet cowl, and fan-jet cowl surfaces, shown in Fig. 4. Good correlation has been achieved in this case.

NAL-AERO-02-01 Turbine-Powered Simulator Model[19]

This geometric configuration is an axisymmetric fan-jet engine nacelle model used in the Turbine-Powered Simulator (TPS) experiment. The contour curves of this geometry, in a two-dimensional plane, were taken from Ref. 19. A half-body configuration was simply constructed by rotation around the axis. The geometry and the grid at the meridian plan are shown in Fig. 5. The constructed grid consists of four blocks. For this powered engine nacelle major boundary surfaces include spinner, fan inlet, fan cowl, fan-jet inner cowl, fan-jet exit, core-jet outer cowl, core-jet inner cowl, core-jet exit, and core-jet spinner.

The numerical simulation has been performed at $M = 0.8$, $\alpha = 0.0$ deg with the following engine conditions: MFR $= 0.497$, BR $= 1.822$, total pressure ratio and total temperature ratio of fan and core jets are 1.343, 0.921, 1.109, and 0.612, respectively, which were taken from the experimental data.

Figure 6 shows pressure distributions on the outer cowl, fan-, and core-cowl surfaces. Comparison shows that the computational results represented by solid line agree very well with the experimental data denoted by symbols.

Flow Simulation for Advanced Twin-Engine Aircraft

To validate the numerical method, two transport aircraft configurations consisting of low-wing/fuselage with wing-mounted pylon/nacelles were chosen for analyses. To get detailed information on the interference effects, the wing surface-pressure distributions are shown in the analyses.

Prototype Model of Transport Aircraft NASA-TP-3168[21]

A sketch of this model is shown in Fig. 7. The engine nacelle is installed at the wing 40% semispan location. The flow-through nacelle represents a very high bypass ratio or superfan engine nacelle. The two primary components of the nacelle are the fan cowl and the centerbody. Figure 8 shows the surface grid of this model. The field

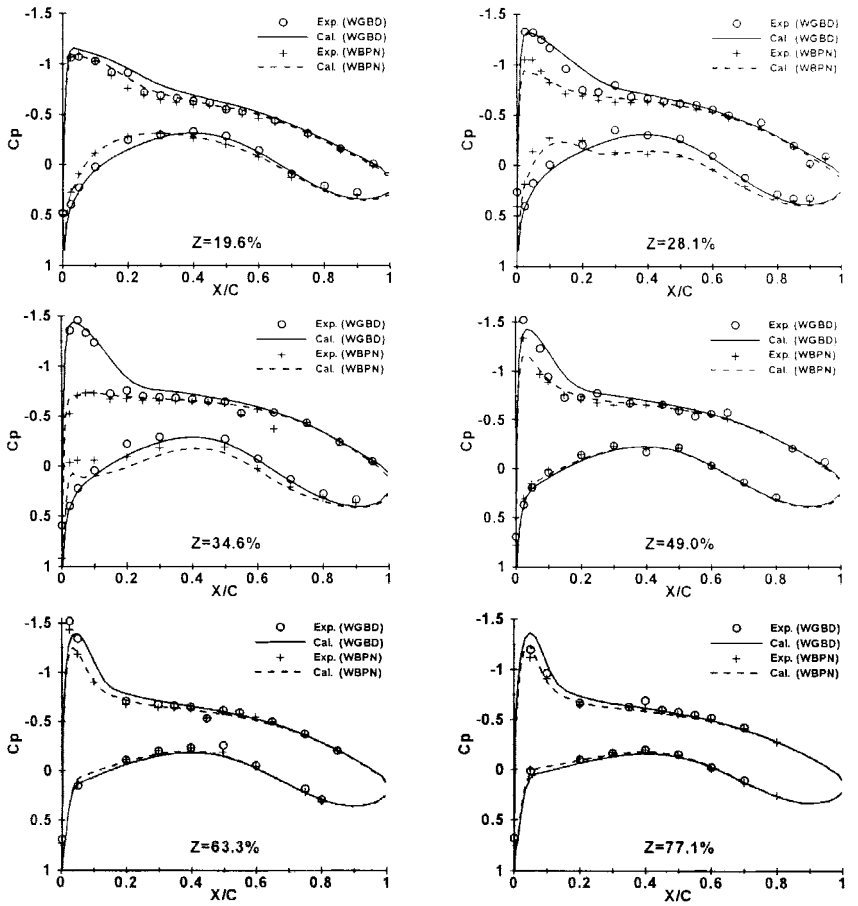

Wing/Body Configuration (WGBD): $M = 0.698, \alpha = 3.16^\circ$; Wing/Body/Pylon/Nacelle Configuration (WBPN): $M = 0.696, \alpha = 2.5^\circ$

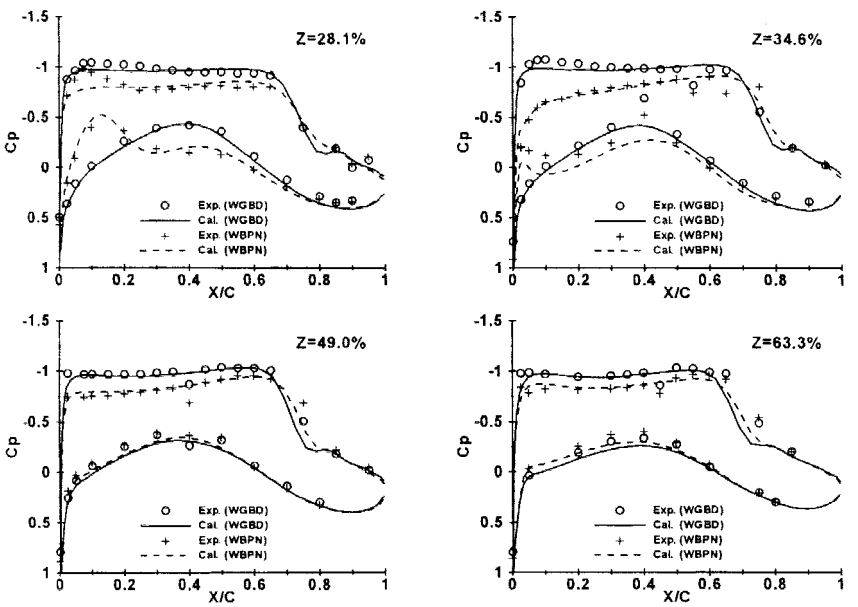

Wing/Body Configuration: $M = 0.82, \alpha = 3.0^\circ$; Wing/Body/Pylon/Nacelle Configuration: $M = 0.82, \alpha = 2.45^\circ$

Fig. 14 Wing surface-pressure distributions for AE100 model.

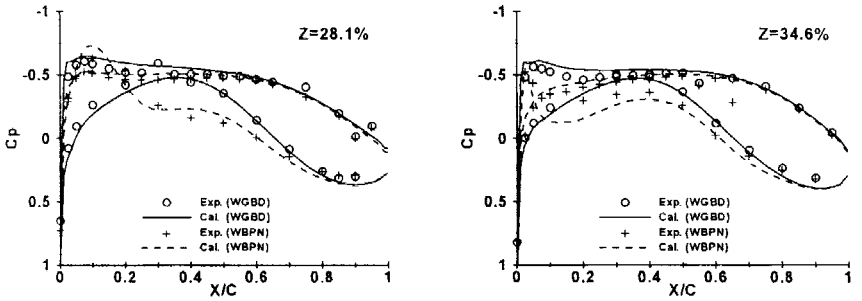

WGBD: $M = 0.705, \alpha = 0.08°$; WBPN: $M = 0.692, \alpha = -0.105°$

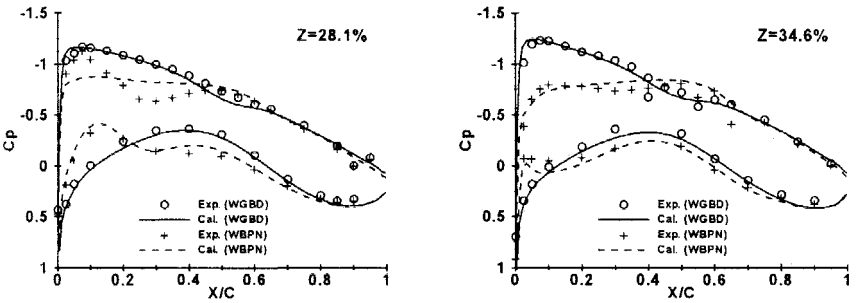

WGBD: $M = 0.777, \alpha = 2.75°$; WBPN: $M = 0.778, \alpha = 2.5°$

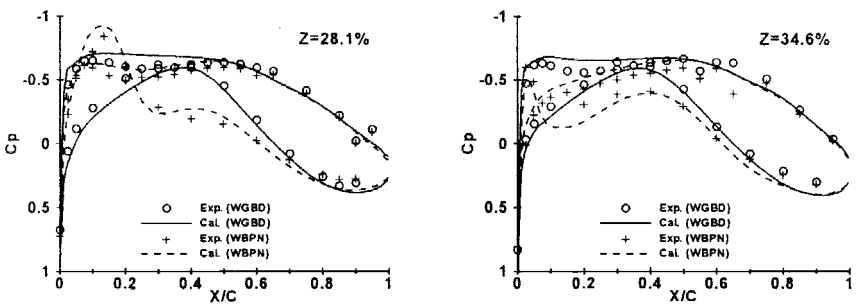

WGBD: $M = 0.78, \alpha = 0.0°$; WBPN: $M = 0.78, \alpha = 0.0°$

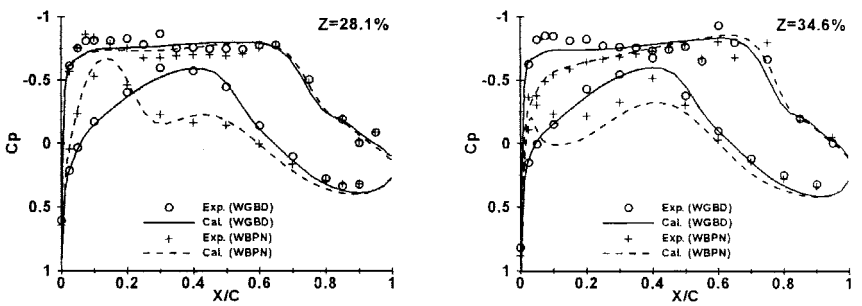

WGBD: $M = 0.815, \alpha = 1.43°$; WBPN: $M = 0.822, \alpha = 1.65°$

Fig. 14 Wing surface pressure distributions for AE100 model (Continued).

grids at different stations along the body axis direction are shown in Fig. 9. The complete field grid for the wing/body/pylon/nacelle configuration is about 750,000 grid points in total, corresponding to 78 points around each of 50 spanwise airfoil sections.

The analysis was performed at the cruise condition $M = 0.77$, $\alpha = 0.9$ deg, and $Re = 2.5 \times 10^6$. Detailed comparisons are provided in Fig. 10, where the computational surface-pressure distributions are compared to the experimental data along several span stations. The computed results are in general agreement with the experimental data.

Twin-Engine, Low-Wing Transport Aircraft Model for Chinese AE100 Project

The aircraft model for Chinese AE100 project is a representation of 115-passenger, twin-engine transport with supercritical wing. The geometry of this model is shown by the surface grid in Figs. 11 and 12. The engine nacelle is installed at the 31.4% wing semispan location. Sketch of the flow-through engine nacelle, which represents a current-technology turbofan, is shown in Fig. 13. The two primary components of the nacelle are the fan cowl and the core cowl.

The pylon/nacelle can be installed on the wing in two possible ways: 1) the symmetrical plane of the engine nacelle is vertical to the horizontal plane, and 2) the symmetrical plane of the engine nacelle is vertical to the wing plane. For the test model the pylon/nacelle is mounted using 1) because of the structural requirements and constrains.

The analyses were carried out at different Mach numbers and angles of attack for the WGBD and the WBPN configuration, respectively. The Reynolds number is about 2.5×10^6. Figure 14 displays comparisons between the computational and the experimental

Table 1 Computed aerodynamic coefficients for WGBD and WBPN

Computing conditions			WGBD		WBPN (1)		WBPN (2)	
M_∞	α	Re	C_l	C_d	C_l	C_d	C_l	C_d
0.696	2.50	2.5×10^6	0.4700	0.0370	0.4514	0.0500	0.4521	0.0483
0.778	2.35	2.5×10^6	0.4830	0.0407	0.4655	0.0504	0.4665	0.0469
0.820	2.45	2.4×10^6	0.4990	0.0510	0.4815	0.0602	0.4795	0.0542

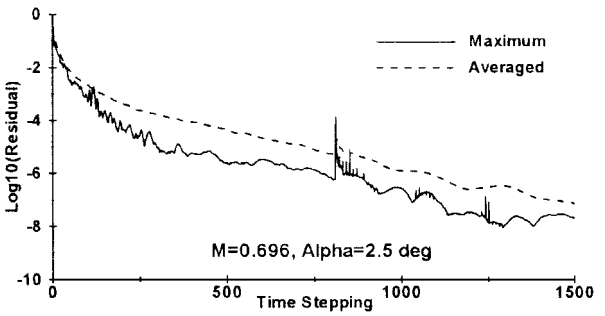

Fig. 15 Convergence history for WBPN computing.

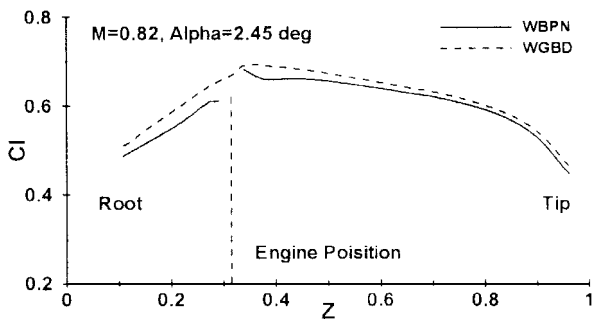

Fig. 16 Wing lift distribution in spanwise direction.

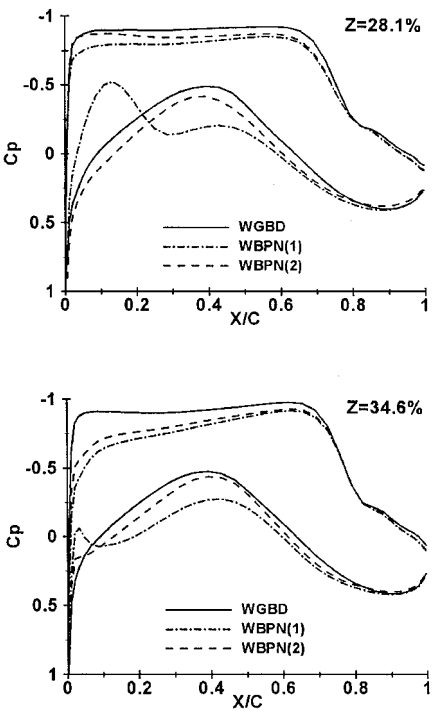

Fig. 17 Comparisons of wing surface-pressure distributions with and without pylon/nacelle ($M = 0.82$, $\alpha = 2.45$ deg).

results. The wing surface-pressure distributions agree with the experimental data very well. This indicates that the computation is well able to account for the interference effects. The demonstration has been made that the simulation method in this study is accurate and efficient. Figure 15 shows the convergence history for the WBPN computing when $M = 0.696$, $\alpha = 2.5$ deg.

Figure 16 displays a comparison of the variation of local lift in the spanwise direction for the WGBD and the WBPN configuration at $M = 0.82$, $\alpha = 2.45$ deg. The configuration with installed nacelle shows a significant loss of lift compared to the clean configuration. At the pylon location the discontinuity in the lift distribution is caused by the fact that on the wing lower surface the pylon separates the flowfield between in- and outboard side. The difference in the pressure distribution in- and outboard of the pylon is responsible for this discontinuity.

The comparisons of the WGBD and the WBPN results show that the installation of the pylon/nacelle has a significant influence on the flowfield over the wing.

The analyses indicate that it is necessary to modify the wing surface near the pylon station, or the pylon surface shape, or the specific installation of the pylon/nacelle on the wing.

Effect of the Pylon/Nacelle Installations for AE100 Model

The effect of the pylon/nacelle installations for AE100 model was also analyzed. Table 1 gives comparisons of some computed aerodynamic coefficients for the WGBD and the WBPN with different pylon/nacelle installation. The comparisons indicate that the installation interference of the pylon/nacelle for the WBPN (2) is decreased. Figure 17 shows comparisons of wing pressure distributions in the sections just in- and outboard of the pylon at $M = 0.82$, $\alpha = 2.45$ deg. For the WBPN (2) the pressure profile inboard of the pylon remains the same as the wing/body combination, thus the induced drag will be less than (1).

Conclusions

This paper describes a numerical technique for simulating the flows around powered engine nacelle and/or advanced transport aircraft with wing-mounted flow-through nacelles. The method is based on a multiblock point-matched grid-generation approach combined with zonal solving strategy for complex flowfields. The computing practice shows that the use of H-type grid topology and the finite volume Euler solver coupled with boundary-layer code is very effective, accurate and reliable for analyzing the complex flowfields in the investigation of airframe/propulsion integration.

In this paper only the flow-through nacelle models are investigated in the transport aircraft examples because of a lack of available data for the case of the wing/body combination with pylon and powered engine nacelle. However, from the validation of the simulation method, there are sufficient reasons to believe that further development will provide a useful engineering tool for the aerodynamic analysis of practical transport aircraft configuration in optimizing the design of the airframe/propulsion integration. Using the numerical simulation, the design risk and costs will be reduced greatly at an early project state.

The numerical calculations in the current study were performed on a Microcomputer Pentium II 400. For a full aircraft it usually takes about 10 min of CPU time to generate a complete multiblock grid, but requires a time-consuming manual geometry definition process (about 2–3 days). In general, the flow simulation needs about 10 h of CPU time for approximately 1500 time steps to converge. In the

light of flow analysis, the present method has high efficiency and demands less computer memory and CPU time than the unstructured grid approach, which often provides a powerful tool for the grid generation about more complex configurations.

Several problems will have to be addressed in the future. The most important of these are 1) the prediction and analysis of large separated zones and 2) grid refinement and computation reduction.

References

[1]Burgsmüller, W., Hoheisel, H., and Kooi, J. W., "Engine/Airframe Interference on Transport Aircraft with Ducted Propfans," International Council of the Aeronautical Sciences, 94-3.7.1, Sept. 1994.

[2]Rill, S., and Becker, K., "Simulation of Transonic Inviscid Flow over a Twin Jet Transport Aircraft," AIAA Paper 91-0025, Jan. 1991.

[3]Rossow, C.-C., and Ronzheimer, A., "Investigation of Interference Phenomena of Modern Wing-Mounted High-Bypass-Ratio Engines by the Solution of the Euler-Equations," AGARD Symposium on Aerodynamic Engine/Airframe Integration, AGARD-CP-498, Oct. 1991.

[4]Rossow, C.-C., Godard, J. L., Hoheisel, H., and Schmitt, V., "Investigations of Propulsion Integration Interference Effects on a Transport Aircraft Configuration," AIAA Paper 92-3097, July 1992.

[5]Rossow, C.-C., and Hoheisel. H., "Numerical Study of Interference Effects of Wing-Mounted Advanced Engine Concepts," International Council of the Aeronautical Sciences, 94-6.4.1, Sept. 1994.

[6]Lynch, F. T., and Intemann, G. A., "The Modern Role of CFD in Addressing Aircraft/Engine Integration Issues for Subsonic Transports," International Council of the Aeronautical Sciences, 94-6.4.3, Sept. 1994.

[7]Gea, L. M., Halsey, N. D., and Intermann, G. A., "Applications of the 3-D Navier–Stokes Code OVERFLOW for Analyzing Propulsion/Airframe Integration Related Issues on Subsonic Transports," International Council of the Aeronautical Sciences, 94-3.7.4, Sept. 1994.

[8]Sonar, T., "Grid Generation Using Elliptic Partial Differential Equations," Deutsche Forschungs- und Versuchsanstalt für Luft- und Raumfahrt Institut für Entwurfsaerodynamik Braunschweig, DFVLR Rept. FB 89-15, March 1989.

[9]Higenstock, A., "A Fast Method for the Elliptic Generation of Three Dimensional Grids with Full Boundary Control," *Numerical Grid Generation In Computational Fluid Mechanics '88*, Pineridge, Swansea, Wales, U.K., 1988, pp. 137–146.

[10]Jameson, A., Shmidt, W., and Turkel, E., "Numerical Solution of the Euler Equations by Finite Volume Methods Using Runge–Kutta Time-Stepping Schemes," AIAA Paper 81-1259, June 1981.

[11]Volpe, G., and Jameson, A., "Efficient Solution for Computing Transonic and Supersonic Flows about Aircraft," International Council of the Aeronautical Sciences, *Journal of Aircraft,* Vol. 27, No. 3, 1990, pp. 223–231.

[12]Whitfield, D. L., and Thomas, J. L., "Transonic Viscous-Inviscid Interaction Using Euler and Inverse Boundary-Layer Equations," *Computational Methods in Viscous Flows*, Vol. 3, *Recent Advances in Numerical Methods in Fluids Series*, edited by Habashi, W. G., Pineridge Press, Concordia University, Montreal, Canada, 1984, pp. 451–474.

[13]Whitfield, D. L., Suafford, T. W., and Jacocks, J. L., "Calculation of Turbulent Boundary Layers with Separation and Viscous/Inviscid Interaction," *AIAA Journal*, Vol. 19, No. 10, 1981, pp. 1315–1322.

[14]Li, F. W., and E, Q., "Numerical Solutions of Transonic Airfoil Flows by Interaction of Euler and Boundary-Layer Equations," *Acta Aerodynamic SINCA*, Vol. 11, No. 1, 1993, pp. 49–56.

[15]Carter, J. E., "A New Boundary Layer Inviscid Iteration Technique for Separated Flow," AIAA Paper 79-1450, July 1979.

[16]Chen, H. C., Yu, N. J., and Rubbert, P. E., "Flow Simulation for General Nacelle Configurations Using Euler Equations," AIAA Paper 83-0539, Jan. 1983.

[17]Hirose, N., Asai, K., Ikawa, K., and Kawamura, R., "3-D Euler Flow Analysis of Fan-jet Engine and Turbine Powered Simulator with Experimental Comparison in Transonic Speed," AIAA Paper 89-1835, June 1989.

[18]Li, J., E, Q., Li, F. W., and Chen, H. X., "3-D Flow Simulations for General Powered Engine Nacelles Using Euler Equations," AIAA Paper 98-0929, Jan. 1998.

[19]Hirose, N., Asai, K., and Ikawa, K., "Transonic 3-D Euler Analysis of Flows Around Fan Jet Engine and Turbine Powered Simulator," National Aerospace Lab., NAL-TR-1045 (Japan), Tokyo, Japan, Nov. 1989.

[20]Kiock, R., and Hoheisel, H., "Design of Axi-Asymmetric Nacelle for the Counter Rotating Ultra-High-Bypass Fan Simulator," Deutsche Forschungsanstalt für Luft- und Raumfahrt Institut für Entwurfsaerodynamik Braunschweig, DLR Rept. FB 93-52, 1993.

[21]Pendergraft, O. C., Ingraldi, A. M., Re, R. J., and Kariya, T. T., "Installation Effects of Wing-Mounted Turbofan Nacelle-Pylons on a 1/17-Scale, Twin-Engine, Low-Wing Transport Model," NASA TP-3168, March 1992.